Journal of
Materials Chemistry A

Accepted Manuscript

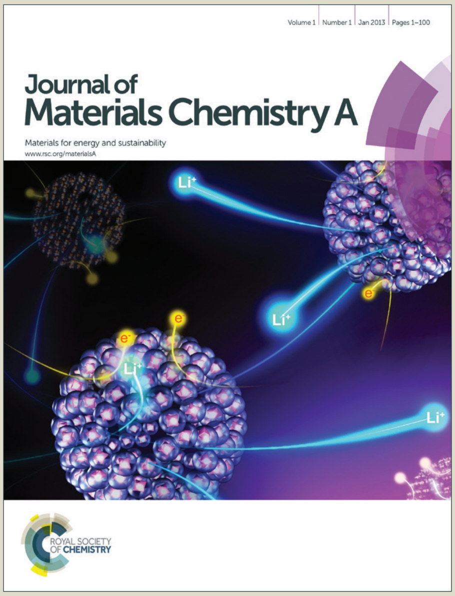

ROYAL SOCIETY
OF **CHEMISTRY**

www.rsc.org/materialsA

Preparing $Bi_{12}SiO_{20}$ crystals at low temperature through nontopotactic solid-state transformation and improving its photocatalytic activity by etching

Qiaofeng Han,[a,*] Juan Zhang,[a] Xin Wang and Junwu Zhu[*]

ABSTRACT

Well-crystalline bismuth silicon oxide ($Bi_{12}SiO_{20}$; BSO) particles were prepared from the reaction of Na_2SiO_3 (or SiO_2) and bismuth oxo compound such as $Bi(NO_3)_3$, α-Bi_2O_3, $(BiO)_2CO_3$ or BiO*X* (*X* = Cl, Br) in alkaline aqueous solution at 70 ℃ for 3 h, whereas conventional syntheses from melt necessitate above 650 ℃. All the reactions from different bismuth precursors experienced the same intermediate α-Bi_2O_3 to the final product BSO with cubic or triangular pyramidal shape, depending upon NaOH concentration and Bi/Si molar ratio. Although the photocatalytic efficiency of the obtained BSO microcrystallites was poor due to large particle size and the associated low specific surface area, we successfully overcame the disadvantage of insufficient active sites on the surface of the BSO microcrystallites through etching. The etched BSO crystals possessed rough surface and exhibited enhanced photocatalytic activity for RhB degradation under visible light irradiation. Specially, the uniform egg-tart shaped BiOCl hierarchical microstructures assembled by nanosheets were produced by tuning etchant concentration, looking like man-made solar energy acceptor, which exhibited superior activity for RhB decomposition under visible light as comparison to its precursor BSO.

1. Introduction

Bismuth-based compounds including Bi_2O_3, $Bi_2Ti_2O_7$, Bi*OX* (*X* = Cl, Br, I), Bi_2WO_6, $BiVO_4$, $BiFeO_3$, $(BiO)_2CO_3$, and so forth, have recently attracted more attention for their photocatalytic activity and potential application in environment remedies and energy conversion due to their suitable band structures, high chemical and optical stability. As a member of bismuth-containing oxides, $Bi_{12}SiO_{20}$ (denoted as BSO) is a conventional photorefractive and electro-optic material for various optical devices including optical data processing, real time intensity inversion, subtraction, image correction with four wave mixing techniques, and so on.[1-7] BSO belongs to Sillenite group with a pseudo-body centered cubic unit cell and the noncentrosymmetric space group *I*23. BSO should theoretically be a candidate for potential application in photocatalysis due to good photoconductivity and suitable band gap energy (2.6 eV).[8] However, photocatalytic performance of BSO has been rarely reported possibly because of its low BET specific surface area resulting from the conventional preparation method. BSO single crystals are commonly grown by the Czochralski (Cz) technique or by hydrothermal treatment at 390 ℃ for 20 days.[7,9,10] BSO ceramics are generally prepared via solid-state reaction (SSR) at 650-750 ℃. BSO powders and nanofibers have been synthesized by molten salt method and electrospinning routes followed by calcination, respectively.[11,12] As for the reported wet chemical methods such as co-precipitation, sol-gel process and chemical solution decomposition, a calcination step is required to develop full crystallinity and phase purity.[8,13,14] All these preparation methods give rise to serious particle agglomeration, poor dispersity and low surface area. He *et al*. reported that the BSO powders exhibited similar photocatalytic activity to P25 TiO_2 even though it possessed a much lower specific surface area (4.87 m^2/g) than P25 (50 m^2/g).[8] Therefore, it is expected that the photocatalytic activity of BSO can be further improved by increasing its surface area. These motivate us to develop a low-temperature method to prepare BSO crystals from the viewpoint of the foundational research and technological application. In this work, we report, for the first time, the synthesis of the phase pure BSO crystals by using a solution crystallization method at a temperature as low as 70 ℃ for 3 h without involvement of calcination.

Triggered by great success of graphene, two-dimensional (2D) sheetlike structures have attracted considerable attention due to their high surface percentage and the unprecedented functionalities.[15] As a photocatalyst, 2D nanosheets can diminish the light block effect and guarantee fast interfacial charge transfer, thus improving the light utilization and promoting photoinduced charge separation. Pumera *et al* claimed that the properties of layered transition chalcogenides in their bulk states vastly differ from their exfoliated counterparts in the nanoscale regime.[16] Considering that the as-synthesized BSO microcrystallites were composed of close-packed sheets, we tried to improve their surface area and photocatalytic activity through selective etching in mixed HCl/HAc solution. Specially, the egg-tart shaped BiOCl hierarchical microstructures (denoted as H-BOC) assembled by loosely-packed nanosheets were firstly prepared by adjusting etching reaction parameters. Since no surfactants were used, the sheetlike H-BOC were surface active and exhibited excellent photocatalytic activity for the degradation of Rhodamine B (RhB) under visible light irradiation.

2. Experimental Section

Samples preparation

All chemicals were of analytical grade and used without further purification. $Bi(NO_3)_3 \cdot 5H_2O$, Na_2SiO_3, NaOH, Rhodamine B (RhB), HCl and glacial acetic acid (HAc) were all purchased from Sinopharm Chemical Reagent Corp. (Shanghai, China). α-Bi_2O_3 and $(BiO)_2CO_2$ was prepared according to our previous work.[17,18]

The BSO powders could be synthesized directly from the precursor $Bi(NO_3)_3$. In a typical procedure, 2 mmol of $Bi(NO_3)_3 \cdot 5H_2O$ (0.97 g) and 0.17 mmol of Na_2SiO_3 (0.05 g) were added into 30 mL of NaOH solution (3 M) in a 100 mL glass bottle under magnetic stirring. The flask was then placed in a water bath at 70 ℃ for 3 h with constant stirring. The color of the mixture changed from white to yellow, finally into pale yellow, indicating that the intermediate Bi_2O_3 was firstly produced, and then into the final product BSO. The product was separated by centrifugation, then washed several times with deionized water and ethanol, and finally dried at 60 ℃ for 12 h. No additional thermal treatment was needed. Alternatively, the BSO powders could also be prepared via a facile solid-liquid phase reaction from the other bismuth precursors like α-Bi_2O_3, Bi*OX* (*X* = Cl, Br) or $(BiO)_2CO_3$ under similar experimental conditions.

The etching reaction was carried out at room temperature under ambient conditions. 200 mg of BSO powders were separated in 5 mL of HAc and ultrasonicated for 5 min, and then a mixed solution of concentrated HCl (37%) and

HAc with a certain volume ratio was cautiously added to the above solution under stirring. After that, the mixture was centrifugated to get rid of acids in order to obtain the etched BSO, or otherwise, the mixture was diluted with about 20 mL of water to prepare H-BOC. The resulting precipitates were collected by washing with ethanol and deionized water thoroughly and drying at 60 ℃ in air.

Characterization

The X-ray diffraction patterns (XRD) were obtained on a Bruker D8 Advance X-ray diffractometer (Cu Kα radiation, λ = 1.542 Å) at a scan rate of 0.05° 2θ s^{-1}. Raman spectra were measured in Renishaw Invia spectrometer. Transmission electron microscopy (TEM) and high resolution TEM (HRTEM) were carried out on a JEM-2100 (JEOL) microscope equipped with equipped with an EDAX energy dispersive X-ray spectrometer (EDS). Scanning electron microscopy (SEM) was preformed on a JSM-5610LV microscope. A Quanta Chrome Nova 1000 analyzer was employed to measure the Brunauer-Emmett-Teller (BET) surface areas of the samples at liquid nitrogen temperature. X-ray photoelectron spectroscopy (XPS) measurements were carried out on a PHI Quantera Ⅱ SXM X-ray photoelectron spectrometer with monochromatized Al Kα as the exciting source, and the results obtained in the XPS analysis were corrected by referencing the C 1s line to 284.8 eV. The UV-Vis diffuse reflectance spectra (DRS) of the products were determined on a shimadzu UV 2550 spectrophotometer equipped with an integrating sphere, using $BaSO_4$ as a reference.

Photocatalytic activity test

The photocatalytic activity of BSO or H-BOC catalysts was evaluated by RhB degradation at the natural pH value. The catalyst powders (0.02 g) were dispersed in 50 mL of RhB (5 ppm) aqueous solution under continuous stirring, allowing 1 h in the dark to reach the adsorption-desorption equilibrium between the dye and catalyst. Visible light irradiation using xenon lamp (500 W) with a 420 nm cutoff filter were applied to the suspension with continuous stirring. At a given time interval, about 4 ml of the suspension was taken out, the powders were removed by centrifugation, and residual RhB concentration in the solution was measured by using a UV-Vis spectrophotometer (BRAIC UV 1201).

3. Results and discussion

Structures, composition and morphology of $Bi_{12}SiO_{20}$

The crystal structure of the as-prepared BSO was checked by XRD. As displayed in Fig. 1, all of the reflections can be indexed to cubic phase $Bi_{12}SiO_{20}$ (JCPDS No. 37-0485) with cell parameters a = 10.107 Å. There are no diffraction peaks from any impurities, indicating that the product is of high purity. The intensity and shape of the peaks show that the product should be well crystalline. Considering that BSO is structurally related to γ-Bi_2O_3 (JCPDS No. 71-0467), both of which belong to Sillenite group with a body-centered cubic unit cell, XRD patterns of bulk BSO and γ-Bi_2O_3 are revealed in Fig. 1. All the diffraction peaks of the as-prepared BSO obviously deviate from the positions of the standard γ-Bi_2O_3, which confirms that the obtained product is not γ-Bi_2O_3 but BSO. Raman, EDS and XPS spectra further demonstrate the presence of element silicon in the product, as discussed below.

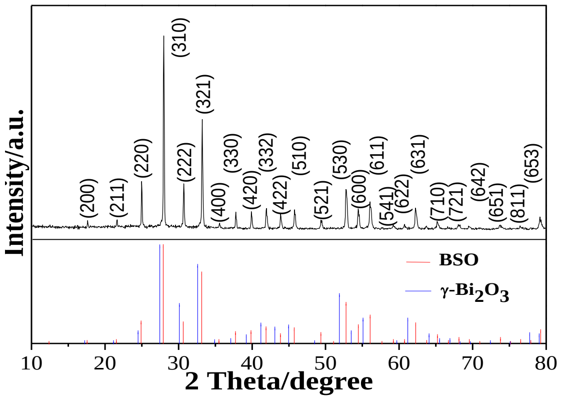

Figure 1 XRD pattern of the as-prepared BSO particles, and vertical sticks below the pattern representing the standard diffraction data from JCPDS file for bulk BSO (No. 37-0485) and γ-Bi_2O_3 (No. 71-0467).

Raman spectra of the as-prepared BSO crystals in the frequency range 100-1000 cm^{-1} are shown in Fig. 2. All the modes of SiO_4 and Bi_3O_4 units are Raman active in the BSO crystal lattice, and their corresponding Raman peaks situation are in good agreement with the literature values.[19-21] The vibration peaks intensity of the SiO_4 tetrahedron are much weaker than those of Bi-O because the tightly bound SiO_4 tetrahedron is surrounded by “a sphere” of twelve heavy bismuth atoms.

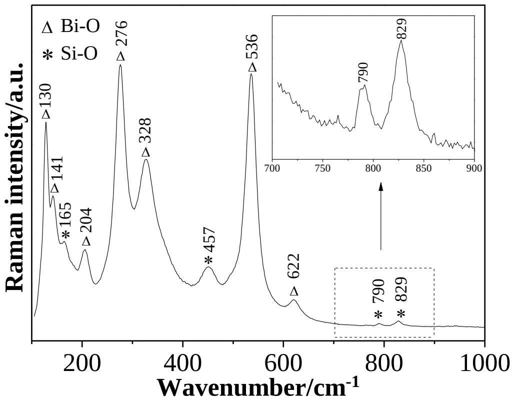

Figure 2 Raman spectra of the as-prepared BSO crystals.

EDS analysis based on TEM image shows the presence of Bi, Si and O elements in the product with a molar ratio of approximately 22:1:2 (Fig. S1), deviating from stoichiometric ratio of $Bi_{12}SiO_{20}$, which reveals that the main contribution to the EDS spectra is given by heavy bismuth atoms. Quantitative EDS analysis is less accurate to light atoms like C, N, O because they possess longer characteristic wavelength of X-ray, which has been seriously absorbed before reaching the detector, and their X-ray fluorescence yield is lower as well.[22]

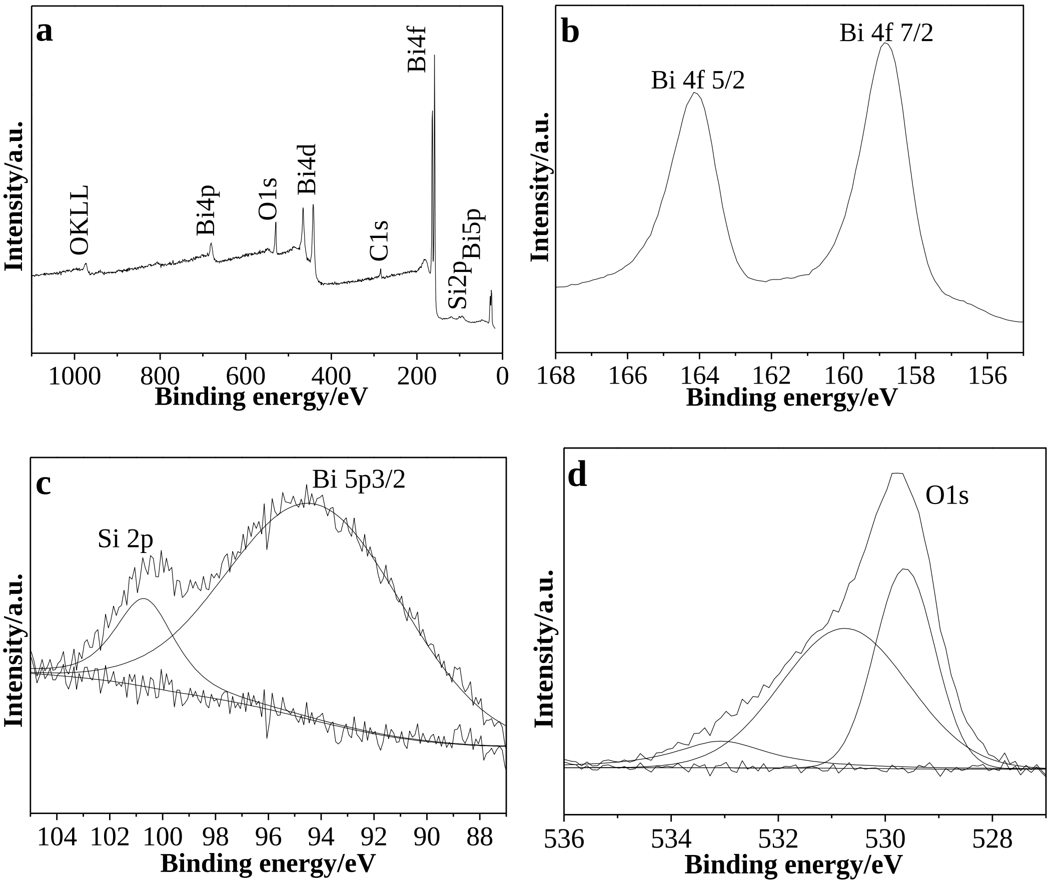

Figure 3 XPS spectra of the as-prepared BSO particles: (a) survey, (b) Bi 4f , (c) Si 2p, and (d) O

1s.

The surface elemental composition and chemical state of the as-prepared BSO was checked by using XPS spectra. No obvious impurities were detected in the survey spectrum except for adventitious carbon (Fig. 3a). The two peaks at 158.8 and 164.1 eV respectively correspond to the binding energies of Bi $4f_{7/2}$ and Bi $4f_{5/2}$ core level (Fig. 3b). The Si 2p peak centered at 100.8 eV is partially overlapped with the Bi $5p_{3/2}$ photoemission at the high binding energy side (Fig. 3c). The O 1s spectra show obvious asymmetry in tails toward the high binding energy side. From the Gaussian-based O 1s spectra deconvolution, three peaks at 529.6, 530.8, and 533.0 eV can be assigned to the binding energies of Si-O, Bi-O and surface hydroxyl groups (or adsorbed H_2O) (Fig. 3d), respectively. All of the binding energy values of Bi 4f, O 1s and Si 2p coincide with those of the reported BSO.[12] Quatification of the XPS peaks gives the molar ratio of Bi:Si:O in the product as 12:1.8:22, indicative of a slight excess of Si and O on the surface in contrast to the given formula $Bi_{12}SiO_{20}$. In addition, quantification analysis based on XPS spectra is more sensitive to light atoms as comparison to EDS.

The morphology of the as-synthesized BSO was characterized by electron microscopy. Fig. 4a shows a typical SEM image of BSO cubes (denoted as C-BSO) produced from the reaction between $Bi(NO_3)_3$ and Na_2SiO_3 in NaOH (3M) solution at 70 ℃ for 3 h. The uniform BSO microcubes with an edge length around 4 μm are highly dispersive with smooth surface. A high-magnification SEM image from a broken cube indicates that C-BSO cube was composed of closely-packed nanosheets (circled area in Fig. 4b). Some small irregular particles present in the product may be due to imperfect growth and crystallization. TEM observation further demonstrates cubic shape with sharp corners (inset in Fig. 4b).

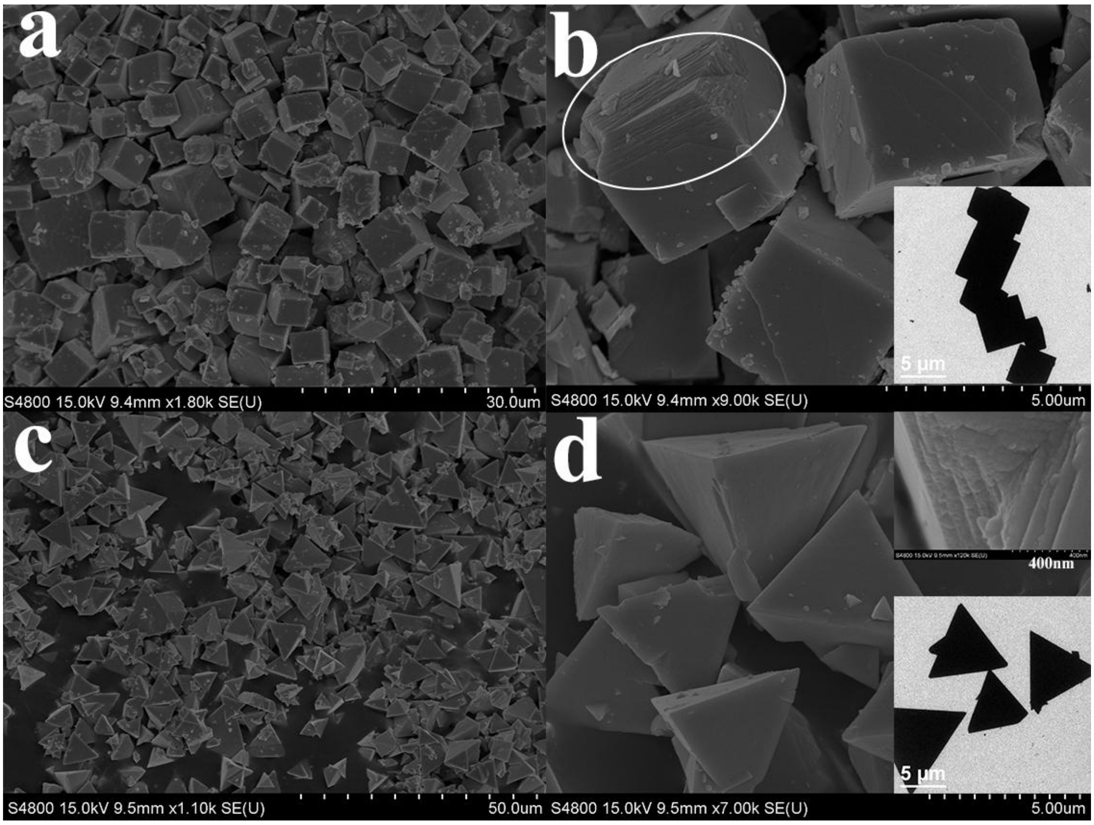

Figure 4 SEM images of the BSO prepared from the reaction of $Bi(NO_3)_3$ and Na_2SiO_3 with a Bi/Si molar ratio of 12:1 at different concentration of NaOH solution: (a) and (b) 3 M, and the inset in (b) is a TEM image; (c) and (d) 5 M, the upper right inset in (d) is a high magnification SEM image of a broken section of a triangle pyramid, and the lower right inset in (d) is a TEM image.

Influencing factors of $Bi_{12}SiO_{20}$ crystals growth

To better understand the growth mechanism of the BSO microcrystallites, a series of experiments were conducted to determine the role of each parameter. The effect of reaction time, reaction temperature, NaOH concentration and types of bases and precursors were evaluated. If the reaction time was shorted to 1 h while keeping other conditions unchanged, XRD pattern and TEM observation reveal that the product corresponds to monoclinic α-Bi_2O_3 (JCPDS No. 65-2366) with rod-like morphology (Fig. S2a). The length of Bi_2O_3 microrods were shortened after 80 min of reaction and short rods became coexistent with cubes. Besides, a large amount of small particles were present in the product (Fig. S2b). After another 10 min of reaction, Bi_2O_3 microrods almost completely disappeared and many cubes can be observed (Fig. S2c). Only BSO cubes can be observed as the reaction time extending to 2 h (Fig. S2d). Therefore, the number of the cubes was increased at the expense of the rods, and α-Bi_2O_3 is an intermediate. As the reaction time was prolonged from 3 to 10 h, the crystallinity, morphology and size of the product remained almost unaltered, suggesting that Ostwald ripening did not occur during this period. The absence of Ostwald ripening means that the current reaction was not a kinetically controlled reaction but a thermodynamically controlled one.[23]

The reaction temperature also influenced the growth of BSO crystals. If lowering the temperature to room temperature, no reaction occurred even when the reaction time was prolonged to 24 h or NaOH concentration was increased to 5 M. When the reaction proceeded at 50 ℃ for 3 h in 3 M of NaOH solution, only rod-like Bi_2O_3 was produced (Fig. S2e). However, if NaOH concentration increasing to 5 M, the BSO began to generate (Fig. S2f), and the pure BSO could be obtained when further prolonging the reaction time to 5 h. Therefore, the activation temperature of this reaction is about 50 ℃, and also, a synergetic effect among OH^- concentration, reaction time and temperature plays a key role in preparing pure BSO.

NaOH concentration is one of the dominant parameters for the generation of phase pure BSO crystals. When NaOH concentration was lower than 2 M (i.e. molar ratio of $OH^-/Bi^{3+} = 30$), the product mainly contains rod-like α-Bi_2O_3 after 3 h of reaction. While, if the reaction time was prolonged to 24 h, the phase pure BSO could be obtained even when NaOH concentration was as low as 1.5 M. In addition, NaOH concentration also influences the morphology of BSO crystals. The BSO triangle pyramids (denoted as T-BSO) appeared as NaOH concentration increasing to above 4 M. When NaOH concentration was more than 5 M, the product mainly existed in pyramidal shape (Fig. 4c and d). A high-resolution SEM image from a broken section of a triangle pyramid shows that it was aggregated by nanosheets (upper right inset in Fig. 4d), analogous to C-BSO. A TEM image further confirms that the particles are regular triangle with sharp tips (lower right inset in Fig. 4d), suggesting that they consist of four equilateral triangle cones. Several irregular particles are also found but they are minority. The XRD patterns also substantiate the shape evolution (Fig. S3). The intensity ratio of the (220)/(222) peaks for C-BSO is higher than that of T-BSO, indicating the difference of the exposed facets between two samples, which is in agreement with the electron microscope observation.

The formation of BSO cubes should be due to its intrinsic crystal growth habit because BSO belongs to cubic phase. The cube is bounded by {100} planes. If the {111} facets are stabilized by adsorption adventitious molecules in order to reduce the total surface energy of the system, this gives rise to the passivation of the {111} facets, forming pyramidal shape. Herein, the structural rearrangement during crystallization was mainly influenced by NaOH concentration. In analogy with organic surfactants, the selective adsorption of OH^- onto surface of BSO crystals would lead to an adjustment of the growth rate ratio between {100} and {111} facets.[24,25] Moreover, the solubility of BSO particles increases with NaOH concentration increasing, which leads to fast growth and subsequent extrinsic pyramidal shape.[26]

When using KOH as a mineralizer, a lower concentration than NaOH is workable to the generation of phase pure BSO owing to stronger basicity. If employing saturated NH_3•H_2O or hexamethylenetetramine (HMTA) as a base source, no reaction occurred due to their weak base strength. Relatively, the amount of Na_2SiO_3 has almost no effect on the purity but morphology of the product. Keeping NaOH concentration at 3 M, the shape of BSO crystals changes from the cubes to the pyramids as the Bi/Si molar ratio was increased from 12/1 to 24/1. According to the common ion effect, the solubility of BSO in solution decreased with SiO_3^{2-} concentration increasing, and so the growth rate decreased, which would result in the formation of BSO with intrinsic cube morphology because slow growth prefers thermodynamically more stable morphology. Growth kinetics plays an important role in the shape control of nanocrystals. He group also reported that the growth of BSO crystals changed from that with {111} and {112} facets mainly presented to that with

{110} and {100} facets mainly presented due to the common ion effect.[9]

Furthermore, when using $(BiO)_2CO_3$ instead of $Bi(NO_3)_3$ as bismuth source, the pure BSO could be prepared at 70 ℃ in 1.5 M of NaOH solution (Fig. S4a). Also, the reaction experienced the intermediate α-Bi_2O_3, as evidenced by the color change of the solution from white to yellow, eventually to pale yellow. As shown in Fig. S4b and c, BSO also present the cubic and pyramidal shapes, depending on NaOH concentration and Bi/Si molar ratio. Besides, if using Bi*OX* (*X* = Cl, Br) as bismuth precursor, pure BSO could be easily prepared, analogous to the case of the precursor $(BiO)_2CO_3$ (Fig. S4d and e). Surely, when directly using α-Bi_2O_3 as bismuth source, pure BSO crystals could be obtained (Fig. S4f).

Finally, the effect of silicon source on the formation of BSO was investigated. Pure BSO crystals could be produced when using SiO_2 as a silicon source. Nevertheless, the longer reaction time was required (5 h) because SiO_2 firstly needed to be transformed into Na_2SiO_3 in the present of NaOH.

Liu group demonstrated the formation of $Bi_2O_2CO_3$, BiOCl, and Bi_2S_3 from topotactic transformation of β-Bi_2O_3 under an acid environment because Bi_2O_3 could only be etched by the acid.[27] In this case, the reaction proceeded in alkaline solution and no morphological and structural similarity from $Bi_2O_2CO_3$ or BiOBr to α-Bi_2O_3 and from α-Bi_2O_3 to BSO were present, and therefore, this topotactic conversion mechanism is not considered here. The production of the intermediate α-Bi_2O_3 from $Bi(NO_3)_3$ in alkaline solution is in agreement with our previous work.[17] The generation of α-Bi_2O_3 from layered Bi*OX* and $(BiO)_2CO_3$ may follow the ion exchange mechanism reported by Zhang *et al.*,[28] where OH^- anions substitute interlayer CO_3^{2-} or halogen to break the stoichiometric layered structure and simultaneously form the non-stoichiometric counterparts like $Bi_{12}O_{15}X_6$, Bi_3O_4X, and finally to Bi_2O_3, because interlayer CO_3^{2-} or halogen is active during chemical reaction. The transformation from the monoclinic α-Bi_2O_3 into the bcc BSO may be due to some crystal planes in Bi_2O_3 (d_{BO}) correlative with those in BSO (d_{BSO}) in the d values. For example,

$$d_{BO(031)} = d_{BSO(400)} = 2.530 \text{ Å}$$

$$d_{BO(320)} = d_{BSO(611)} = 1.640 \text{ Å}$$

And also, α-Bi_2O_3 with the d-spacings of the $\{-112\}_{BO}$, $\{-211\}_{BO}$ and $\{-132\}_{BO}$ facets is 2.386, 2.149 and 1.838 Å, respectively, close to that of the $\{330\}_{BSO}$, $\{332\}_{BSO}$ and $\{521\}_{BSO}$ facets. XRD patterns intuitively indicate the presence of some overlapped peaks between α-Bi_2O_3 and BSO (Fig. S5). These may lead to the transformation of α-Bi_2O_3 into BSO. α-Bi_2O_3 may act as a sacrificial template for the product BSO, or in other words, BSO microcrystallites may grow epitaxially from the α-Bi_2O_3 rods. The more exact mechanism still puzzles us and further study is underway. Up to now, there are no reports on the formation of BSO at so low temperature.

Selective etching for $Bi_{12}SiO_{20}$ and formation of BiOCl

The specific surface areas of the as-prepared T-BSO and C-BSO are 0.47 and 0.89 m^2/g, respectively, as calculated from nitrogen adsorption measurement using the Brunauer-Emmet-Teller method (Fig. S6a and b). The large grain size and the associated low surface area are the main aspects to be improved in order to obtain higher photocatalytic activity. Therefore, the BSO microcrystallites were etched by carefully adjusting experimental parameters. After etching for about 1 min in HCl/HAc (0.1 M) solution, the surface of the C-BSO cubes (denoted as et-C-BSO) changed noticeably rough together with the appearance of substantial amounts of debris (Fig. 5a and b). The individual layers do not clearly delaminate and remain as stacked macrostructures, indicative of incomplete exfoliation. XPS spectra of the et-C-BSO indicate that the binding energies values of Bi 4f, O 1s and Si 2p are in good agreement with the parent C-BSO (Fig. S7), whereas, an increase in the relative intensity of the Si 2p peaks relevant to Bi 5p confirms the Bi removal from the lattice by etching. A trace amount of element Cl was detected, implying that the impurity BiOCl may be present on the surface of BSO. Nevertheless, no BiOCl crystal phase could be measured from XRD pattern (Fig. S8a), indicative of phase purity of the et-C-BSO. The amount of the impurity BiOCl should be sufficiently low to be undetectable by XRD. If using H_2O instead of HAc as etching solvent, a small amount of impurity BiOCl appeared from XRD measurement (Fig. S8b). The BiOCl came from the combination of Cl^- and BiO^+ in the presence of water, as discussed below.

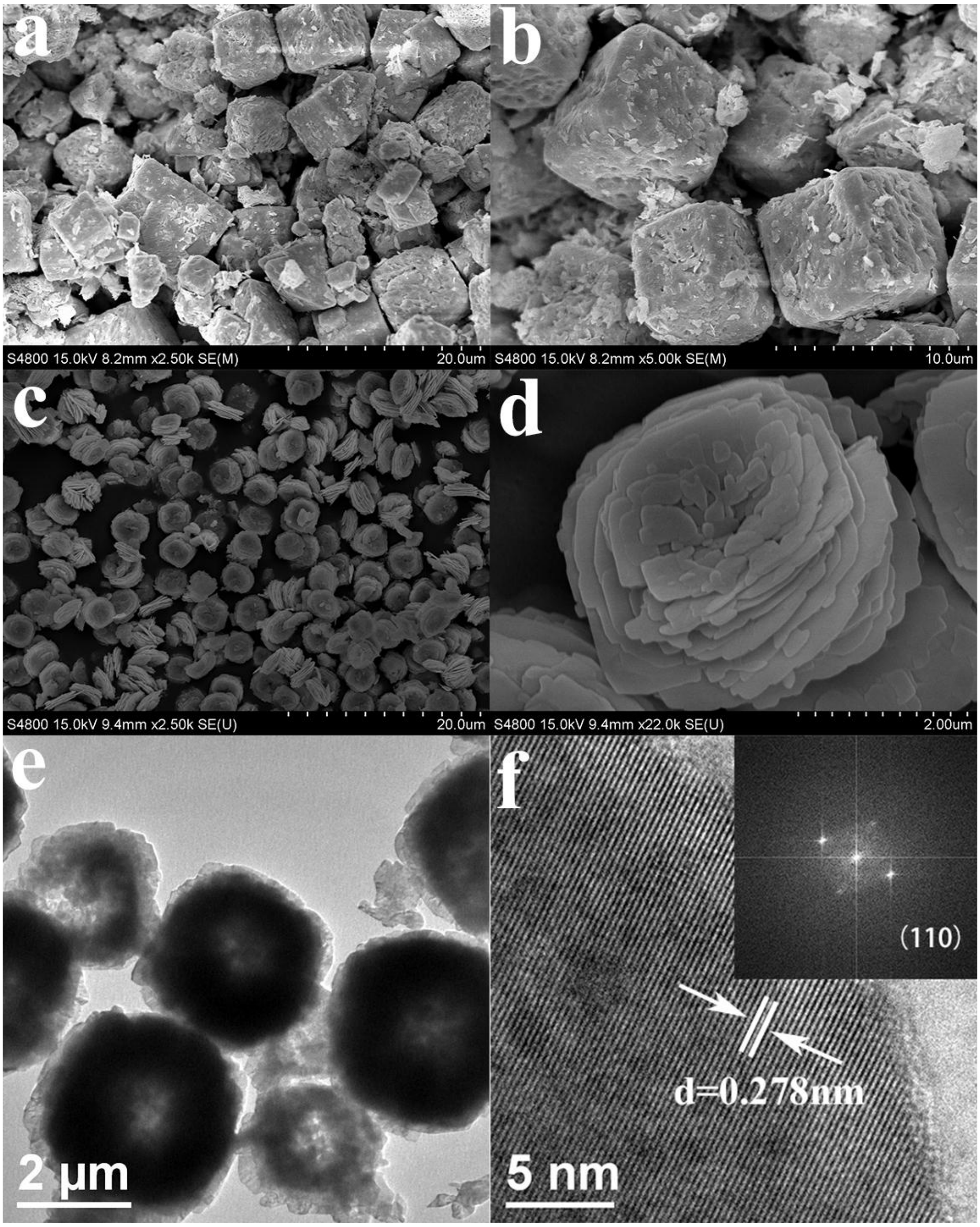

Figure 5 SEM images (a-d) of the etched BSO samples: (a) et-C-BSO, (b) a high resolution SEM image of et-C-BSO, (c) H-BOC, (d) a high resolution SEM image of H-BOC; (e) TEM image of H-BOC, (f) HRTEM image of H-BOC, and the inset in (f) is its FFT pattern.

In contrast, the etched product obtained from the parent T-BSO (denoted as et-T-BSO) under the same experimental conditions is less rough on the surface (Fig. S9a), suggesting that the T-BSO surrounded by {111} facets was thermodynamically more stable because the {111} facets have the lowest surface energy in cubic crystals.[29] In addition, the surface coarsening of both C-BSO and T-BSO was increased with etchant concentration or etching time increasing, and at the same time, the impurity BiOCl increased.

When HCl concentration was increased to 1.2 M (volume ratio of HCl/HAc is 1:9), the BSO powders were almost completely dissolved. If the deionized water was added into this reaction system, the white precipitate was instantly produced and after 3 min of stirring, the phase pure tetragonal BiOCl was obtained (Fig. S10). SEM observation indicates that the BiOCl presents uniform egg-tart shaped hierarchical architectures (denoted as H-BOC) with an average diameter of 2 μm (Fig. 5c). All the microflowers are of the same size and are highly dispersive. An amplified SEM image reveals that each microflower is composed of 2D nanosheets with a thickness of approximately 40 nm (Fig. 5d). These nanosheets with smooth surface are close-packed from center to edge and loose-packed layer by layer to form egg-tart shaped architectures, each containing a concavity on its center. A TEM image of the microflowers indicates the distinct contrast between the center and edge, which further confirms that the egg-tart shaped H-BOC are thinner at the centers (Fig. 5e). An HRTEM image of an individual nanosheet indicates continuous and clear fringes. The spacing of the adjacent lattice planes is 0.278 nm, which is consistent with the interplanar spacing of (110) planes of tetragonal BiOCl (Fig. 5f). Both HRTEM image and FFT pattern (inset of Fig. 5f) demonstrate that the nanosheet is single crystalline in nature. In addition, there is no obvious morphology difference between two BiOCl crystals prepared from C-BSO and T-BSO.

XPS spectra of H-BOC indicate that the binding energies of Bi 4f, O 1s and Cl 2p are in good agreement with pure BiOCl (Fig. S11).[30] According to the quantitative analysis of XPS peak areas, the molar ratio of Bi:O:Cl is 1:1.1:1, close to stoichiometric BiOCl. XPS measurement shows that the element Si content is less than 0.1% for H-BOC sample.

As $[Bi_3O_4]^+$ can be dissolved in HCl solution, the etching reaction may be estimated by the following equations (Eq.).

$$Bi_3O_4^+ + 8H^+ \rightarrow 3Bi^{3+} + 4H_2O \qquad (1)$$

$$CH_3COO^- + H^+ \rightarrow CH_3COOH \qquad (2)$$

$$Bi^{3+} + H_2O \rightarrow BiO^+ + 2H^+ \qquad (3)$$

$$BiO^+ + Cl^- \rightarrow BiOCl \qquad (4)$$

$$Bi_{12}SiO_{20} + 12HCl + 4HAc \rightarrow 12BiOCl + 8H_2O + Si\text{-}(\text{-}Ac)_4 \qquad (5)$$

The etching reaction quickly proceeded even in very diluted HCl solution (Eq. (1)). HAc may serve as a buffer reagent during the etching reaction (Eq. (2)). Large quantities of BiO^+ was produced in the presence of water (Eq. (3)), and thus readily resulted in the generation of BiOCl (Eq. (4)). The element Si may be removed by two routes. One possibility is that HAc may act as complexing agent to bind Si-OH and removed Si atoms away from the lattices (Eq. (5)).[31] Grabmaier and Oberschmid proposed that the Si-OH may exist in the $Bi_{12}SiO_{20}$ lattice due to the substitution of the OH^- for an O(3) site from adjacent $SiO(3)_4$ tetrahedra.[32] The other is that amorphous SiO_2 particles may suspend in the solution and were removed by centrifugation.

The volume ratio of HCl/HAc influenced the morphology of BiOCl crystals. When HCl concentration increased to 6 M (HCl/HAc; v/v = 1:1), dispersed BiOCl nanosheets (denoted as S-BOC) with a thickness of about 30 nm were obtained (Fig. S9b), which resulted from fast growth and nucleation rate due to high HCl concentration.

The formation of BOCl sheetlike nanostructures should be attributed to its intrinsic layer structure characteristics. Although various methods have been reported to prepare the BiOCl hierarchitectures,[28] up to now, it is the first time to synthesize the egg-tart shaped BOCl microstructures in such a short time at room temperature without any surfactants.

The surface area of et-C-BSO increases to 3.22 m^2/g (Fig. S6d, Table 1), which should result in enhanced photocatalytic activity. Besides, H-BOC possesses a higher surface area and porosity as compared to the reported BiOCl microstructures (Fig. S6f, Table 1),[30] which could be ascribed to its complex hierarchical architectures.

Optical properties and photocatalytic activity

Diffuse reflectance spectroscopy (DRS) is a useful tool to characterize the electronic states in optical materials. Fig. 6 and Fig. S12 illustrate the absorption spectra of the as-prepared BSO as well as BOC samples, which were transformed from the DRS according to the Kubelka-Munk theory.[25] The absorbance edge of the samples C-BSO and T-BSO located at approximately 450 and 480 nm, respectively, which are in accordance with their pale yellow and green yellow color. Both of the et-C-BSO and et-T-BSO samples show two band-edge absorptions, one at 450-480 nm and the other at 390-400 nm. Lee *et al*. also observed two band-edge-gap structure for N-doped $(BiO)_2CO_3$.[33] In this case, the band-edge at 450-480 nm is for intrinsic BSO, whereas, the band-edge at 390-400 nm should be due to the existence of the impurity BiOCl at the surface. The H-BOC shows absorption edge at the near-UV region (~385 nm), which is in good agreement with the reported values.[28,30] Both BSO and BOC belong to semiconductors with an indirect band gap.[8,34] The band gap energies (E_g) can be estimated from the plot of $(\alpha hv)^{1/2}$ versus hv (α: absorption coefficient; hv: photo energy) by extrapolating the linear portion of the curve to $\alpha = 0$ (Table 1).

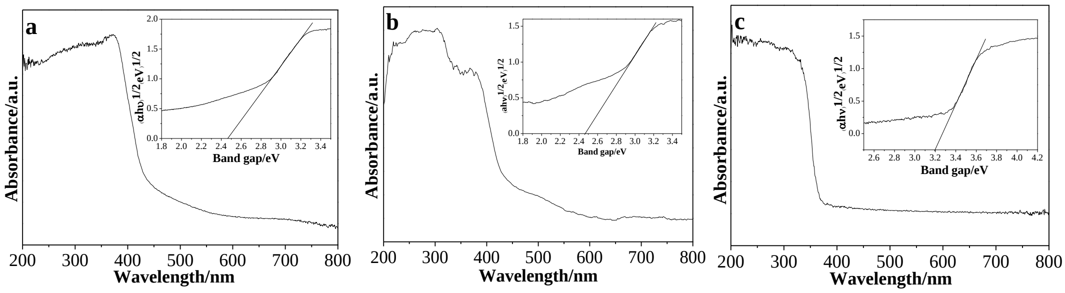

Figure 6 DRS spectra of the samples: (a) C-BSO, (b) et-C-BSO, and (c) H-BOC; the inset showing the plots of $(\alpha hv)^{1/2}$ versus photon energy (hv).

Before photocatalytic activity measurement, we examined the adsorption process of RhB over the BSO and BOC samples in the dark (Fig. S13). The results reveal that the adsorption-desorption reached the equilibrium in 40 min over all the samples. The etched BSO possess higher RhB adsorption capacity than before etching (Table 1), which could be attributed to the surface area factor. In addition, the adsorption capacity of both BiOCl samples is relatively higher than the etched BSO, which may be relevant to their sheetlike structures.

Table 1 Surface area, pore volume and band gap energy of the samples, adsorption capacity for RhB, and apparent rate constant *k* for RhB photodegradation

Samples	Surface area (m^2 g^{-1})	Pore volume/10^{-3} (cm^3 g^{-1})	Band gap (eV)	Adsorption capacity (mg g^{-1})	$K/10^{-4}$ (min^{-1})
T-BSO	0.47	1.2	2.32	0.17	5.66
C-BSO	0.89	1.3	2.46	0.30	8.89
et-T-BSO	1.22	6.9	2.28	0.46	14.2
et-C-BSO	3.22	14.4	2.47	2.64	79.9
S-BOC	4.56	11.7	3.24	5.32	728
H-BOC	2.86	7.6	3.25	3.58	960

The photocatalytic activity of the BSO powders before and after etching was investigated through decomposition of RhB under visible light irradiation. For comparison, the photodegradation of RhB without catalyst (blank) was also studied. The temporal evolution of the absorption spectra of RhB over the catalysts under visible light irradiation is shown in Fig. S14. The time-dependent degradation rate of RhB over the studied photocatalysts is shown in Fig. 7A, where C_0 represents the initial concentration of RhB after adsorption-desorption equilibration and C denotes

RhB concentration at a certain irradiation time. It can be seen that negligible degradation of RhB occurred within 100 min of visible light irradiation without any photocatalyst (blank). The absorbance evolution of RhB over all of the BSO powders with irradiation time shows that there is a decrease of the absorption band strength without shifting of the maximum absorbance wavelength at about 554 nm during the whole photodegradation, indicating that RhB could be degraded over BSO catalysts via photocatalysis process without photosensitization process, which are in accordance with their band gap energies. Nevertheless, only limited RhB can be degraded over C-BSO and T-BSO catalysts (Fig. 7Aa and b), which may be due to their low surface area. The C-BSO presents slightly higher photocatalytic activity than T-BSO, implying that the {001} facets of BSO are more reactive than the thermodynamically more stable {111} facets, analogous to their etching reaction activity. The photocatalytic activity of the et-C-BSO was greatly improved, as shown in Fig. 7Ad, and the degradation rate of RhB reaches 61% after 100 min of visible light irradiation. In contrast, the degradation rate is low (about 13%) over the et-T-BSO (Fig. 7Ac), which might be due to its poor etching extent and the associated low surface area (Table 1). The degradation rate of RhB over etched T-BSO increased to 65% when the etching extent was intensified by extending the etching reaction time or increasing etchant concentration (Fig. S15). Given that the RhB photodegradation follows the pseudo-first-order mechanism, the apparent degradation rate constant (k) of the et-C-BSO is higher than that of C-BSO (Fig. 7Bb and d, Table 1). The k value normalized by the surface area for et-C-BSO is 25×10^{-4} g min^{-1} m^{-2}, higher than that for C-BSO (10 ×10^{-4} g min^{-1} m^{-2}), indicating that photocatalytic activity of BSO is not only related to the surface structure but also the surface area.

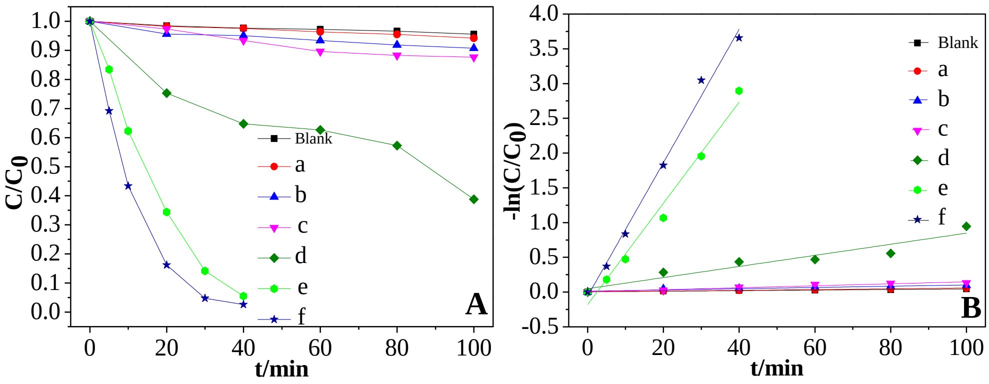

Figure 7 (A) Photocatalytic efficiency and (B) kinetic linear simulation curves of RhB degradation under visible light over various catalysts: (a) T-BSO, (b) C-BSO, (c) et-T-BSO, (d) et-C-BSO, (e) S-BOC and (f) H-BOC.

The presence of BiOCl catalysts resulted in obvious degradation of RhB (Fig. 7Ae and f), and degradation rate of RhB within 40 min over H-BOC and S-BOC reach 100 and 95%, respectively. The absorbance evolution of RhB over both of BOC samples with irradiation time shows that there is a decrease of the absorption band without shifting of the maximum absorbance wavelength at about 554 nm at the beginning (Fig. S14e and f), indicative of the degradation of the conjugated structure of RhB due to a photocatalytic process. However, after 10, 20 and 30 min of illumination, the absorption peak is respectively blue-shifted to 548, 532 and 514 nm in addition to its global decrease, indicating that the N-de-ethylation of RhB occurred. That is to say, RhB initially tetra-ethylated becomes tri, di-, and mono-ethylated,[35] and finally completely degraded in 40 min. These results signified that RhB could be degraded over BOC via photocatalysis process together with the photosensitization process, which is relevant to its large band gap energy (3.25 eV). The slight degradation rate of the SA over H-BOC under visible light further substantiates this analyses (Fig. S16), because colorless salicylic acid (SA) cannot be excited by visible light and the photosensitization degradation process could not take place. During photosensitization degradation, the close contact between dye molecules and photocatalyst is prerequisite for the injection of photoexcited electrons into photocatalyst. Theoretically, better photocatalytic activity of S-BOC with higher surface area and adsorption capacity for RhB may be expected. However, the *K* value normalized by the surface area of H-BOC (0.0335 g min^{-1} m^{-2}) is higher than that of S-BOC (0.0159 g min^{-1} m^{-2}), suggesting that the photocatalytic activity of BiOCl nanoparticles is obviously dependent on the morphology. Hierarchical architectures could enhance light utilization significantly because of the multiple reflections of light within the interior structures of the egg-tart shaped BiOCl assembled by layers. For comparison, several reported results on photocatalytic activity of BiOCl catalysts with various shapes are listed in Table S1, from where we can see that the degradation rate of RhB over the as-prepared H-BOC under visible light is higher than that of some of the sheetlike BiOCl microspheres, and moreover, the catalyst dosage in this work is less. Therefore, the egg-tart shaped BiOCl hierarchical microstructures, looking like man-made solar energy acceptor, are more favorable for light absorbance and fast interfacial charge transfer, and subsequent high photocatalytic efficiency.

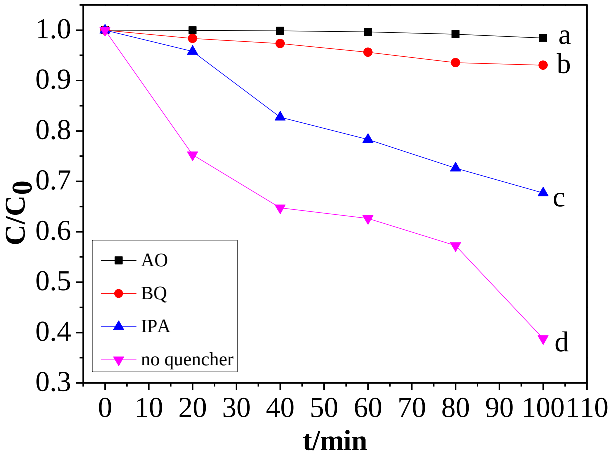

Figure 8 Photodegradation efficiency of RhB over et-C-BSO in the presence of 1 mM of: (a) AO, (b) BQ, (c) IPA and (d) no quencher.

There is few report on photocatalytic mechanism of $Bi_{12}SiO_{20}$ as a photocatalyst. The active species responsible for the degradation of RhB over et-C-BSO catalyst under visible light irradiation were determined by the addition of millimolar concentrations of quenchers in the initial solution under otherwise identical experimental conditions with the RhB degradation without any quenchers. For comparison, an original degradation RhB curve over et-C-BSO without quencher was added. As displayed in Fig. 8, isopropanol (IPA; a quencher of •OH radical) did not significantly affect the degradation of RhB throughout the experiment, which suggests that •OH radicals was the miner active species. This may be due to the standard redox potential of Bi^{V}/Bi^{III} (+1.59 eV) being more negative than that of •OH /OH^{-} (+1.99 eV).[36] On the contrary, the addition of ammonia oxalate (AO; a quencher of h^{+}) exhibited the most evident inhibition to photodegradation of RhB,[37] and besides, 1,4-benzoquinone (BQ; a quencher of superoxide radical) also has a inhibitory effect on the degradation of RhB, indicating h^+ and $\bullet O_2^-$ are main active species involved in this photocatalytic system. It is known that the surface oxygen vacancies are the active sites for the molecular oxygen adsorption, which are capable of capturing photo-induced electrons to generate reactive $\bullet O_2^-$. In BSO crystals, the oxygen vacancies (V_o^+) are generated for charge compensation due to tetrahedrally bonded Bi_{Si}^{3+} ions present in undoped BSO, where a part of the Si sites in the SiO_4 tetrahedron are occupied by Bi^{3+}.[8] During the direct photoexcitation degradation, the valence band of the catalyst is involved in the photoreaction, and so the positive holes become main species of BSO. The active species experiment using H-BOC as a photocatalyst indicate that $\bullet O_2^-$ and positive holes are main species in aqueous solution under visible light (Fig. S17), which is in agreement with the reported BiOCl catalysts.[36]

The catalytic and structural stability of the H-BOC have been studied. The H-BOC photocatalyst has a about 30% decrease in activity after four cycles (Fig. S18). However, the XRD pattern of H-BOC after four cycles still displays the sharp and strong diffraction peaks corresponding to pure tetragonal phase of BiOCl (Fig. S19a), identical to that of the fresh sample. Besides, the sample after the repeated photocatalytic experiments maintains the egg-tart shaped morphology (Fig. S19b), indicating that the BiOCl crystal structures are stable during photocatalysis. The loss of photocatalytic activity was induced by strong adsorption of RhB on the surface of H-BOC catalyst, which can be evidenced by color change of the H-BOC powders from white to rose pink after photocatalytic experiments.

4. Conclusions

This work provides a facile and low-temperature route to synthesize $Bi_{12}SiO_{20}$ cubes and triangular pyramids in NaOH solution from various bismuth compounds. It is believed that all of the reaction from different bismuth oxide precursors experienced the intermediate α-Bi_2O_3. The transformation of α-Bi_2O_3 into $Bi_{12}SiO_{20}$ is due to some matched lattice facets. The photocatalytic activity of the as-prepared $Bi_{12}SiO_{20}$ microcrystallites could be significantly improved through etching reaction. Moreover, the egg-tart shaped BiOCl hierarchical microflowers can be easily fabricated through etching of $Bi_{12}SiO_{20}$ in HCl/HAc solution at room temperature. This kind of BiOCl hierarchical microstructures possess high surface area and porosity, which are favorable for adsorption of dyes, harvest of photo-energy and efficient transport of photo-induced electrons and holes, and therefore, exhibit excellent photocatalytic activity for RhB degradation under visible light. Such an approach can likely be extended to other bismuth composites to not only achieve cost-effective synthesis for practical applications but also to improve reactivity of existing micro/nanostructures.

Acknowledgments

The work is financially supported by the National Natural Science Foundation of China (51372117, 51322212), the Natural Science Foundation of Jiangsu Province (BK20131347), and the Priority Academic Program Development of Jiangsu Higher Education Institutions (PAPD).

Notes and references

Key Laboratory for Soft Chemistry and Functional Materials, Ministry of Education,
Nanjing University of Science and Technology, Nanjing 210094, China
E-mail: hanqiaofeng@njust.edu.cn and zhujw@njust.edu.cn

[a] These authors equally contributed to this work.

† Electronic Supplementary Information (ESI) available: EDS spectra of BSO, XRD and TEM images to track the morphological and structural evolution of the products, nitrogen adsorption-desorption isotherms, XPS spectra of et-BSO, photocatalytic activity evolution of the products and the stability of BSO. See

1 J. Sato, H. Kobayashi, K. Ikarashi, N. Saito, H. Nishiy-ama and Y. Inoue, *J. Phys. Chem. B*, 2004, **108**, 4369.

2 T. I. Milenov, P. A. Botev, P. M. Rafailov and M. M. Gospodinov, Mater. *Sci. Eng. B*, 2004, **106**, 148.

3 J. N. Wooder and J. C. Dainty, *Opt. Commun.*, 1987, **63**, 85.

4 H. Vogt, K. Buse, H. Hesse, E. Krätzig and R. R. Garcia, *J. Appl. Phys.*, 2001, **90**, 3167.

5 J. Herriau and J. Huignard, *Appl. Phys. Lett.*, 1986, **49**, 1140.

6 B. Riscob, M. Shkir, V. Ganesh, N. Vijayan, K. K. Maurya, K. Kishan Rao and G. Bhagavannarayana, *J. Alloy. Compd.*, 2014, **588**, 242.

7 S. Moorthy Babu, K. Kitamura and S. Takekawa, *J. Cryst. Growth*, 2005, **275**, e681.

8 C. He and M. Gu, *Scripta Mater.*, 2006, **55**, 481.

9 X. He, W. Zhou, C. Zhang, H. Zhou, Z. Hu, H. Huo, Y. Zuo, F. Lu, J. Wang, S. Qin, D. Li, H. Zhang and Y. Chen, *J. Cryst. Growth*, 2011, **318**, 900.

10 S. L. Hou, R. B. Lauer and R. E. Aldrich, *J. Appl. Phys.*, 1973, **44**, 2652.

11 J. Lu, X. Wang and H. Jiang, *Mater. Manuf. Process*, 2013, **28**, 126.

12 D. Hou, X. Hu and Y. Wen, *Phys. Chem. Chem. Phys.*, 2013, **15**, 20698.

13 B. J. Jeong, M. R. Joung, S. H. Kweon, J. S. Kim, S. Nahm, J. W. Choi and S. J. Hwang, *Mater. Res. Bull.*, 2012, **47**, 4510.

14 A. Veber, S. Kunej and D. Suvorov, *Ceram. Int.*, 2010, **36**, 245.

15 B. Radisavljevic, A. Radenovic, J. Brivio, V. Giacometti and A. Kis, *Nat. Nanotechnol.*, 2011, **6**, 147.

16 A. Y. S. Eng, A. Ambrosi, Z. Sofer, P. Šimek and M. Pumera, *ACS Nano*, 2014, **8**, 12185.

17 L. L. Yang, Q. F. Han, J. Zhao, J. W. Zhu, X. Wang and W. H. Ma, *J. Alloy. Compd.*, 2014, **614**, 353.

18 L. Yang, Q. Han, J. Zhu and X. Wang, *Mater. Lett.*, 2015, **138**, 235.

19 Y. Hu and D. C. Sinclair, *Chem. Mater.*, 2013, **25**, 48.

20 B. Mihailova, M. Gospodinov and L. Konstantinov, *J. Phys. Chem. Solid*s, 1999, **60**, 1821.

21 W. Wojdowski, *Status Solidi B*, 1985, **130**, 121.

22 J. Goldstein, D. Newbury, D. Joy, C. Lyman, P. Echlin, E. Lifshin, L. Sawyer and J. Michael, *Scanning Electron Microscopy and X-ray Microanalysis*, Springer, New York, 3rd edn., 2003, ch. 1, pp. 1-19.

23 A. Pottier, S. Cassaignon, C. Chanéac, F. Villain, E. Tronc and J. P. Jolivet, *J. Mater. Chem.*, 2003, **13**, 877.

24 G. Dell'Agli, A. Colantuono and G. Mascolo, *Solid State Ionics*, 1999, **123**, 87.

25 Y. Chen, X. Gu, C. G. Nie, Z. Y. Jiang, Z. X. Xie and C. J. Lin, *Chem. Commun.*, 2005, **33**,

4181.

26 X. He, H. Zhou, W. Zhou, Z. Hu, C. Zhang, H. Huo, J. Wang, Y. Zuo and F. Lu, *J. Cryst. Growth*, 2012, **351**, 182.

27 C. F. Guo, J. Zhang, Y. Tian and Q. Liu, *ACS Nano*, 2012, **6**, 8764.

28 J. Li, Y. Yu and L. Zhang, *Nanoscale*, 2014, **6**, 8473.

29 H. J. Yang, S. Y. He, H. L. Chen and H. Y. Tuan, *Chem. Mater.*, 2014, **26**, 1785.

30 S. Weng, Z. Fang, Z. Wang, Z. Zheng, W. Feng and P. Liu, *ACS Appl. Mater. Inter.*, 2014, **6**, 18423.

31 R. K. Iler, *J. Phys. Chem.*, 1952, **56**, 673.

32 B. C. Grabmaier and R. Oberschmid, *Phys. Status Solidi A*, 1986, **96**, 199.

33 F. Dong, S. C. Lee, Z. Wu, Y. Huang, M. Fu, W. K. Ho, S. Zou and B. Wang, *J. Hazard. Mater.*, 2011, **195**, 346.

34 G. Cheng, J. Xiong and F. J. Stadler, *New J. Chem.*, 2013, **37**, 3207.

35 T. Saison, N. Chemin, C. Chanéac, O. Durupthy, V. Ruaux, L. Mariey, F. Maugé, P. Beaunier and J. P. Jolivet, *J. Phys. Chem. C*, 2011, **115**, 5657.

36 L. Ye, K. Deng, F. Xu, L. Tian, T. Peng and L. Zan, *Phys. Chem. Chem. Phys.*, 2012, **14**, 82.

37 Q. Tian, J. Zhuang, J. Wang, L. Xie and P. Liu, *Appl. Catal. A-Gen.*, 2012, **425-426**, 74.

Figure Captions:

Figure 1 XRD pattern of the as-prepared BSO particles, and vertical sticks below the pattern representing the standard diffraction data from JCPDS file for bulk BSO (No. 37-0485) and γ-Bi_2O_3 (No. 71-0467).

Figure 2 Raman spectra of the as-prepared BSO crystals.

Figure 3 XPS spectra of the as-prepared BSO particles: (a) survey, (b) Bi 4f , (c) Si 2p, and (d) O 1s.

Figure 4 SEM images of the BSO prepared from the reaction of $Bi(NO_3)_3$ and Na_2SiO_3 with a Bi/Si molar ratio of 12:1 at different concentration of NaOH solution: (a) and (b) 3 M, and the inset in (b) is a TEM image; (c) and (d) 5 M, the upper right inset in (d) is a high magnification SEM image of a broken section of a triangle pyramid, and the lower right inset in (d) is a TEM image.

Figure 5 SEM images (a-d) of the etched BSO samples: (a) et-C-BSO, (b) a high resolution SEM image of et-C-BSO, (c) H-BOC, (d) a high resolution SEM image of H-BOC; (e) TEM image of H-BOC, (f) HRTEM image of H-BOC, and the inset in (f) is its FFT pattern.

Figure 6 DRS spectra of the samples: (a) C-BSO, (b) et-C-BSO, and (c) H-BOC; the inset showing the plots of $(\alpha h\nu)^{1/2}$ versus photon energy ($h\nu$).

Table 1 Surface area, pore volume and band gap energy of the samples, and apparent rate constant k for RhB photodegradation.

Figure 7 Photocatalytic efficiency of RhB degradation under visible light over various catalysts: (a) T-BSO, (b) C-BSO, (c) et-T-BSO, (d) et-C-BSO, (e) S-BOC and (f) H-BOC.

Figure 8 Photodegradation efficiency of RhB over et-C-BSO in the presence of 1 mM of: (a) AO,

(b) BQ, (c) IPA and (d) no quencher.

A table of contents entry:

The egg-tart shaped BiOCl hierarchitectures with efficient visible-light photocatalytic activity were prepared through etching of $Bi_{12}SiO_{20}$ obtained at low temperature.